PHYSICAL REVIEW B **102**, 024102 (2020)

Origin of mean-field behavior in an elastic Ising model

Layne B. Frechette[1,2] Christoph Dellago,[2,3,*] and Phillip L. Geissler[1,2,†]
[1]*Department of Chemistry, University of California, Berkeley, California 94720, USA*
[2]*Erwin Schrödinger Institute for Mathematics and Physics, University of Vienna, Boltzmanngasse 9, Vienna 1090, Austria*
[3]*Faculty of Physics, University of Vienna, Boltzmanngasse 5, Vienna 1090, Austria*

(Received 22 April 2020; revised 14 June 2020; accepted 18 June 2020; published 6 July 2020)

Simple elastic models of spin-crossover compounds are known empirically to exhibit classical critical behavior. We demonstrate how the long-range interactions responsible for this behavior arise naturally upon integrating out mechanical fluctuations of such a model. A mean-field theory applied to the resulting effective Hamiltonian quantitatively accounts for both thermodynamics and kinetics observed in computer simulations, including a barrier to magnetization reversal that grows extensively with system size. For nanocrystals, which break translational symmetry, a straightforward extension of mean-field theory yields similarly accurate results.

DOI: 10.1103/PhysRevB.102.024102

I. INTRODUCTION

The impact of spin-lattice interactions on materials' phase behavior has long been a topic of interest in condensed-matter physics and materials science [1–4]. Microscopic coupling between spin and geometry in an extended material can endow it with intriguing and useful properties, such as susceptibility of the crystal structure to light or pressure [5–9]. Elastic Ising models provide a minimal representation of such materials. In a simple variant, the atoms of a crystal lattice interact with their neighbors via Hookean springs. The natural length of these springs is determined by the participating atoms' internal "spin" (which could represent either a literal spin state or a chemical identity). This type of model has been employed in studies of lattice-mismatched semiconductor alloys [10,11] and spin-crossover compounds [12,13]. Despite its substantial history, one of the most basic aspects of this model's behavior remains unresolved. The aforementioned studies employed Monte Carlo (MC) simulations to demonstrate that elastic Ising models can exhibit demixing transitions governed by mean-field critical exponents. However, the microscopic origin of this behavior has not been explicitly identified, nor has a quantitative framework for predicting its consequences been developed.

Here, we present a thorough explanation for the origin of this mean-field behavior. Drawing from our recent work on a similar elastic Ising model [14], we show how the coupling of mechanical fluctuations to spins engenders effective interatomic interactions with infinite spatial extent. These give rise to the observed mean-field critical behavior. With an explicit form for the interactions in hand, we develop a straightforward mean-field theory (MFT) which accurately predicts the free energy as a function of magnetization as well as the critical temperature for spontaneous symmetry breaking. MFT yields similarly faithful predictions for relaxation dynamics of the magnetization in the presence of an external field. Finally, we extend our theory to describe spatially heterogeneous systems such as nanocrystals. Our results provide a theoretical basis not only for interpreting the results of a number of previous computer simulation studies but also for the design of switchable elastic materials.

II. ELASTIC ISING MODEL AND EFFECTIVE INTERACTIONS

We consider a collection of N atoms at positions $\mathbf{r}_\mathbf{R} = \mathbf{R} + \mathbf{u}_\mathbf{R}$. The quantity $\mathbf{R}$ denotes a site on a d-dimensional crystal lattice characterized by unit bond vectors $\hat{\boldsymbol{\alpha}}$, and $\mathbf{u}_\mathbf{R}$ is the displacement of an atom from its ideal lattice site. Spin variables $\sigma_\mathbf{R} = \pm 1$ determine the natural bond length between neighboring atoms:

$$l(\sigma_\mathbf{R}, \sigma_{\mathbf{R}+a\hat{\boldsymbol{\alpha}}}) = \begin{cases} l_{AA} \text{ for } \sigma_\mathbf{R} = \sigma_{\mathbf{R}+a\hat{\boldsymbol{\alpha}}} = 1, \\ l_{AB} \text{ for } \sigma_\mathbf{R} \neq \sigma_{\mathbf{R}+a\hat{\boldsymbol{\alpha}}}, \\ l_{BB} \text{ for } \sigma_\mathbf{R} = \sigma_{\mathbf{R}+a\hat{\boldsymbol{\alpha}}} = -1, \end{cases} \tag{1}$$

where a is the fluctuating lattice parameter, $l_{BB} < l_{AA}$, and $l_{AB} = (l_{AA} + l_{BB})/2$. We choose the lattice mismatch $\Delta = (l_{AA} - l_{BB})/2$ to be our basic unit of length. An external pressure p couples directly to the volume cNa^d, where c is a geometry-dependent constant of $O(1)$. The Hamiltonian governing the system is quadratic in deviations of bond lengths $|\mathbf{r}_{\mathbf{R}+a\hat{\boldsymbol{\alpha}}} - \mathbf{r}_\mathbf{R}|$ from their preferred σ-dependent values:

$$\mathcal{H} = \frac{K}{4} \sum_{\mathbf{R},\hat{\boldsymbol{\alpha}}} [|a\hat{\boldsymbol{\alpha}} + \mathbf{u}_{\mathbf{R}+a\hat{\boldsymbol{\alpha}}} - \mathbf{u}_\mathbf{R}| - l(\sigma_\mathbf{R}, \sigma_{\mathbf{R}+a\hat{\boldsymbol{\alpha}}})]^2 + pcNa^d. \tag{2}$$

The spring constant $K > 0$ determines the elastic energy scale $\epsilon = K\Delta^2/8$. We express all quantities henceforth in units of Δ and ϵ. Due to fluctuations in the lattice parameter a, the volume appearing in the final term of Eq. (2) is a random

---

[*] christoph.dellago@univie.ac.at
[†] geissler@berkeley.edu

variable whose statistics are shaped by the externally imposed pressure.

The Hamiltonian defined by Eq. (2) manifestly couples spin and displacement variables. We will show how the effect of fluctuations in the displacements can be captured by an effective energy function $\mathcal{H}_{\text{eff}}$ of the spin variables:

$$\mathcal{H}_{\text{eff}}[\{\sigma_{\mathbf{R}}\}] = \mathcal{H}^{\text{SR}} + \mathcal{H}^{\text{LR}} - h\sum_{\mathbf{R}} \sigma_{\mathbf{R}}, \tag{3}$$

$$\mathcal{H}^{\text{SR}} = \frac{1}{2}\sum_{\mathbf{R},\mathbf{R}'} \sigma_{\mathbf{R}} V^{\text{SR}}_{\mathbf{R}-\mathbf{R}'}\sigma_{\mathbf{R}'}, \tag{4}$$

$$\mathcal{H}^{\text{LR}} = \frac{1}{2N} V^{\text{LR}} \left(\sum_{\mathbf{R}} \sigma_{\mathbf{R}}\right)^2, \tag{5}$$

where SR and LR stand for "short range" and "long range," respectively. $V^{\text{SR}}_{\mathbf{R}}$ is an effective interaction potential that decays steadily with distance $|\mathbf{R}|$, and V^{LR} is a constant that sets the strength of long-range coupling. This form of spin interaction guarantees mean-field critical behavior, as will be discussed below.

We first simplify Eq. (2) by noting that if Δ is small, $\mathcal{H}$ can be written approximately as (see [14] and the Supplemental Material [15])

$$\mathcal{H} \approx 2\sum_{\mathbf{R},\hat{\boldsymbol{\alpha}}} \left[\hat{\boldsymbol{\alpha}}\cdot(\mathbf{u}_{\mathbf{R}+a\hat{\boldsymbol{\alpha}}} - \mathbf{u}_{\mathbf{R}}) - \frac{1}{2}(\delta\sigma_{\mathbf{R}} + \delta\sigma_{\mathbf{R}+a\hat{\boldsymbol{\alpha}}}) - (\tilde{\sigma}_0/N - \delta a)\right]^2 - Nh\delta a, \tag{6}$$

where $h = -pcdl_{AB}^{d-1}$ is dimensionless pressure and $\delta a = a - l_{AB}$. We have partitioned the spin variables into two components, namely, the net magnetization $\tilde{\sigma}_0 = \sum_{\mathbf{R}} \sigma_{\mathbf{R}}$ and the local deviation $\delta\sigma_{\mathbf{R}} = \sigma_{\mathbf{R}} - \tilde{\sigma}_0/N$. Using $\sum_{\mathbf{R}} \mathbf{u}_{\mathbf{R}} = 0$, we expand Eq. (6):

$$\mathcal{H} = \Delta\mathcal{H}(\{\mathbf{u}_{\mathbf{R}}\}, \{\delta\sigma_{\mathbf{R}}\}) + 2(\tilde{\sigma}_0/N - \delta a)^2 NZ - Nh\delta a, \tag{7}$$

where Z is the coordination number of the lattice and

$$\Delta\mathcal{H} = 2\sum_{\mathbf{R},\hat{\boldsymbol{\alpha}}} \left[\hat{\boldsymbol{\alpha}}\cdot(\mathbf{u}_{\mathbf{R}+a\hat{\boldsymbol{\alpha}}} - \mathbf{u}_{\mathbf{R}}) - \frac{1}{2}(\delta\sigma_{\mathbf{R}} + \delta\sigma_{\mathbf{R}+a\hat{\boldsymbol{\alpha}}})\right]^2. \tag{8}$$

Gaussian fluctuations in the lattice parameter δa evidently couple solely to $\tilde{\sigma}_0$. Working in an ensemble with fixed N, p, and inverse temperature $\beta = 1/k_B T$, where k_B is Boltzmann's constant, we integrate out these fluctuations:

$$\bar{\mathcal{H}} = -\beta^{-1}\ln\left[\int d(\delta a)\exp(-\beta\mathcal{H})\right] \tag{9}$$

$$= \Delta\mathcal{H} - h\tilde{\sigma}_0 + \text{const.} \tag{10}$$

We see that h simply plays the role of an effective field acting on $\tilde{\sigma}_0$, so spin coupling is contained entirely in $\Delta\mathcal{H}$. We interrogate this coupling by further integrating out Gaussian fluctuations in the displacement field [dropping the unimportant constant term in Eq. (10)]:

$$\mathcal{H}_{\text{eff}} = -\beta^{-1}\ln\left[\int\prod_{\mathbf{R}} d\mathbf{u}_{\mathbf{R}}\exp(-\beta\Delta\mathcal{H})\right] - h\tilde{\sigma}_0. \tag{11}$$

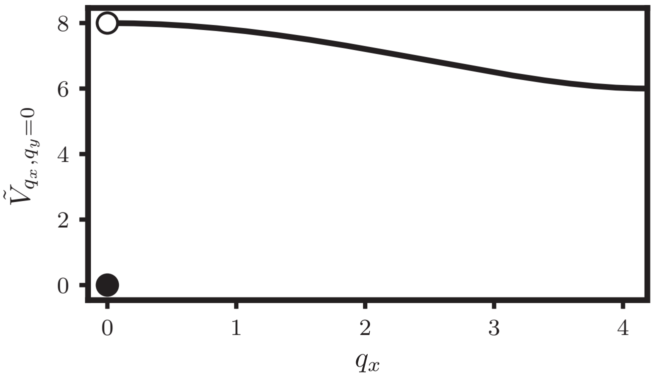

FIG. 1. Fourier-space effective potential for the triangular lattice, Eq. (13). Note that $\tilde{V}_{\mathbf{q}}$ is smooth everywhere except $\mathbf{q} = 0$ since $\tilde{V}_0 = 0$ but $\lim_{\mathbf{q}\to 0}\tilde{V}_{\mathbf{q}} = 8$.

If we assume that our system is subject to periodic boundary conditions, then the required integrals are most easily performed in Fourier space. This yields (see [14])

$$\mathcal{H}_{\text{eff}}[\{\sigma_{\mathbf{R}}\}] = \frac{1}{2N}\sum_{\mathbf{q}} \tilde{V}_{\mathbf{q}}|\tilde{\sigma}_{\mathbf{q}}|^2 - h\tilde{\sigma}_0, \tag{12}$$

where $\tilde{f}_{\mathbf{q}}$ denotes the Fourier transform of a generic function $f_{\mathbf{R}}$ [16]. The explicit form of the effective potential $\tilde{V}_{\mathbf{q}}$ for the triangular lattice is given by [14]

$$\tilde{V}_{\mathbf{q}} = \begin{cases} \frac{4\left(2\cos\frac{q_x a}{2}\cos\frac{\sqrt{3}q_y a}{2} + \cos q_x a - 3\right)^2}{(\cos q_x a - 2)\left(4\cos\frac{q_x a}{2}\cos\frac{\sqrt{3}q_y a}{2} - 3\right) + \cos\sqrt{3}q_y a}, & \mathbf{q} \neq 0, \\ 0, & \mathbf{q} = 0, \end{cases} \tag{13}$$

where q_x and q_y are the Cartesian components of $\mathbf{q}$.

The existence of long-range coupling is not immediately evident from this analysis since the longest-wavelength component of the potential $\tilde{V}_0$ is zero. However, the limit of the potential as $\mathbf{q} \to 0$ is not approached smoothly (see Fig. 1), a required condition for short-range interactions [17,18]. Observe that a simple modification of $\tilde{V}_{\mathbf{q}}$ *does* vanish smoothly as $\mathbf{q} \to 0$:

$$\tilde{V}^{\text{SR}}_{\mathbf{q}} = \tilde{V}_{\mathbf{q}} - (1 - \delta_{\mathbf{q},0})\lim_{\mathbf{q}'\to 0}\tilde{V}_{\mathbf{q}'}. \tag{14}$$

Its inverse transform $V^{\text{SR}}_{\mathbf{R}}$ is therefore a well-defined short-range interaction [19]. The remainder of $\tilde{V}_{\mathbf{q}}$ is

$$\tilde{V}^{\text{LR}}_{\mathbf{q}} = \tilde{V}_{\mathbf{q}} - \tilde{V}^{\text{SR}}_{\mathbf{q}} \tag{15}$$

$$= \text{const} - \delta_{\mathbf{q},0}\lim_{\mathbf{q}'\to 0}\tilde{V}_{\mathbf{q}'}, \tag{16}$$

where the constant term simply generates an irrelevant self-interaction, which we drop. Plugging this back into the sum in Eq. (12) and writing all quantities in terms of real-space sums gives us the promised form (3), with

$$V^{\text{LR}} = -\lim_{\mathbf{q}\to 0}\tilde{V}_{\mathbf{q}}. \tag{17}$$

The limit is given explicitly by

$$\lim_{\mathbf{q}\to 0} \tilde{V}_{\mathbf{q}} = 2Z - 4\mathbf{a}(\hat{\mathbf{q}}) \cdot \mathbf{A}^{-1}(\hat{\mathbf{q}}) \cdot \mathbf{a}(\hat{\mathbf{q}}), \quad (18)$$

$$\mathbf{a}(\hat{\mathbf{q}}) = \sum_{\hat{\boldsymbol{\alpha}}} (\hat{\mathbf{q}} \cdot \hat{\boldsymbol{\alpha}})\hat{\boldsymbol{\alpha}}, \quad (19)$$

$$\mathbf{A}(\hat{\mathbf{q}}) = \sum_{\hat{\boldsymbol{\alpha}}} (\hat{\mathbf{q}} \cdot \hat{\boldsymbol{\alpha}})^2 \hat{\boldsymbol{\alpha}}\hat{\boldsymbol{\alpha}}, \quad (20)$$

where $\hat{\mathbf{q}}$ is an arbitrary unit vector. For the triangular lattice, this simplifies to $\lim_{\mathbf{q}\to 0} \tilde{V}_{\mathbf{q}} = 8$.

III. MEAN-FIELD THEORY

That long-range interactions are operative in spin-crossover compounds has been suggested by several authors [20–25]. Miyashita *et al.* [12] conjectured that the long-range interactions responsible for mean-field behavior in their model had the same $1/|\mathbf{R} - \mathbf{R}'|^3$ decay as that between point defects in three-dimensional continuum elastic media. We have demonstrated that, instead, an infinitely long range interaction arises from a discontinuity in the spectrum $\tilde{V}_{\mathbf{q}}$. This nonanalytic feature originates physically in a mismatch between the elastic energy associated with $\mathbf{q} = 0$ and small (but nonzero) wave vector variations in the magnetization. Schulz *et al.* [26] argued that precisely those long-wavelength elastic modes ought to be responsible for the mean-field behavior of elastic models of binary alloys.

A model which consists solely of interactions of the form $\mathcal{H}^{\mathrm{LR}}$ is described exactly by MFT [27–30]. Its mean-field critical exponents are robust to the addition of short-range ferromagnetic interactions [31–33]. Sufficiently strong interactions encouraging other kinds of order may overwhelm $\mathcal{H}^{\mathrm{LR}}$ and render the mean-field critical point inaccessible [31], which appears to be the case in the recent work of Nishino *et al.* [34]. Short-range interactions added in Ref. [34] to an elastic Hamiltonian much like ours yielded antiferromagnetic ordering whose critical scaling is not mean field in character. We show in the Supplemental Material [15] that adding these same interactions to our effective potential $\mathcal{H}_{\mathrm{eff}}$ similarly shifts the global energy minimum from $\mathbf{q} = 0$ (as in Fig. 1) to a nonzero wave vector consistent with an antiferromagnetic ground state. Absent such added competing interactions, MC simulations of our elastic model for several different lattice structures all yield mean-field critical exponents (see the Supplemental Material [15] for details.) Although it does encourage antiferromagnetic order on the triangular lattice, $\mathcal{H}^{\mathrm{SR}}$ is evidently too weak to impact mean-field universality.

There is no such guarantee for nonuniversal quantities such as the critical temperature T_c, but if the magnitude of $V_{\mathbf{R}}^{\mathrm{SR}}$ is small, then MFT may still predict their values with reasonable accuracy. We obtained such predictions using standard techniques of MFT [35], which yield a self-consistent equation for the net magnetization per atom $m = \tilde{\sigma}_0/N$,

$$m = \tanh(2\beta\bar{V}m + h), \quad (21)$$

as well as a simple expression for the free energy $F(m)$:

$$F_{\mathrm{MF}}(m) = E_{\mathrm{MF}}(m) - TS_{\mathrm{MF}}(m), \quad (22)$$

$$E_{\mathrm{MF}} = -N\bar{V}m^2 - Nhm, \quad (23)$$

$$S_{\mathrm{MF}}/k_B = \ln\binom{N}{N\frac{1+m}{2}} \quad (24)$$

$$\approx -N\left[\frac{1-m}{2}\ln\frac{1-m}{2} + \frac{1+m}{2}\ln\frac{1+m}{2}\right], \quad (25)$$

where $\bar{V} = -\sum_{\mathbf{R}\neq 0} V_{\mathbf{R}}/2$ characterizes both long- and short-range contributions to the mean field. The second expression for S_{MF}, obtained from Stirling's approximation for large N, will be used in mean-field calculations that do not specify system size. When $h = 0$, Eq. (21) implies a critical temperature $T_c = 2\bar{V}$ for spontaneous symmetry breaking.

To test the accuracy of MFT, we performed MC simulations of the elastic Hamiltonian (2) on a periodic triangular lattice. Specifically, we repeatedly proposed changes in a, $\{\mathbf{u}_{\mathbf{R}}\}$, and $\{\sigma_{\mathbf{R}}\}$ and accepted these changes with probabilities designed to satisfy detailed balance (see [15] for details.) Some simulations (described later) were performed using the effective Hamiltonian (12); for these simulations, only changes in $\{\sigma_{\mathbf{R}}\}$ were necessary. We employed umbrella sampling [36] combined with histogram reweighting [37] to compute free energies. In addition, we located T_c from the intersection of Binder cumulants computed at different system sizes [38]. The results agree quantitatively with our mean-field predictions, as shown in Fig. 2. We found similarly excellent agreement between MC and MFT for several different lattice structures in both two and three dimensions [15].

IV. DYNAMICS: QUENCHING AND HYSTERESIS

As a more stringent test of MFT, we consider the dynamics of our elastic Ising model. Free-energy profiles like that in Fig. 2 are suggestive of a time-dependent response that would follow a sudden change in external control parameters. But this relaxation advances in the high-dimensional space of spin configurations, through sequential flips of spins that are correlated in space and in time. Resolving few of these details, MFT asserts that thermodynamic driving forces determine time evolution in a simple way. Its success in a dynamical context would provide powerful tools to predict and understand nonequilibrium response.

The model energy function in Eq. (2) constrains microscopic rules for time evolution but does not specify them uniquely. To craft a dynamical model we must additionally assign rates to microscopic transitions which are consistent with Boltzmann statistics. As a simplification, we take relaxation of the displacement variables $\mathbf{u}_{\mathbf{R}}$ to be much faster than that of spin variables. This rapid mechanical equilibration allows us to consider time variations of the spin field $\sigma_{\mathbf{R}}$ alone, biased by an effective Hamiltonian. In the small-mismatch limit this effective energy is given by Eq. (3). We adopt transition rates $\pi(\sigma_{\mathbf{R}} \to \sigma'_{\mathbf{R}})$ among spin configurations proportional to their Metropolis Monte Carlo acceptance probabilities, $\pi(\sigma_{\mathbf{R}} \to \sigma'_{\mathbf{R}}) = \tau^{-1}\min[1, \exp[-\beta\Delta\mathcal{H}_{\mathrm{eff}}]]$, where τ is an arbitrary reference timescale.

The ordering dynamics that follow a rapid quench from $T > T_c$ to $T < T_c$ are strongly influenced by the long-range component of $\mathcal{H}_{\mathrm{eff}}$. Models with exclusively short-range interactions, such as those described by $\mathcal{H}^{\mathrm{SR}}$, develop finite-wavelength instabilities upon such quenching [39]. These Ising-like instabilities are visually manifest in the coarsening

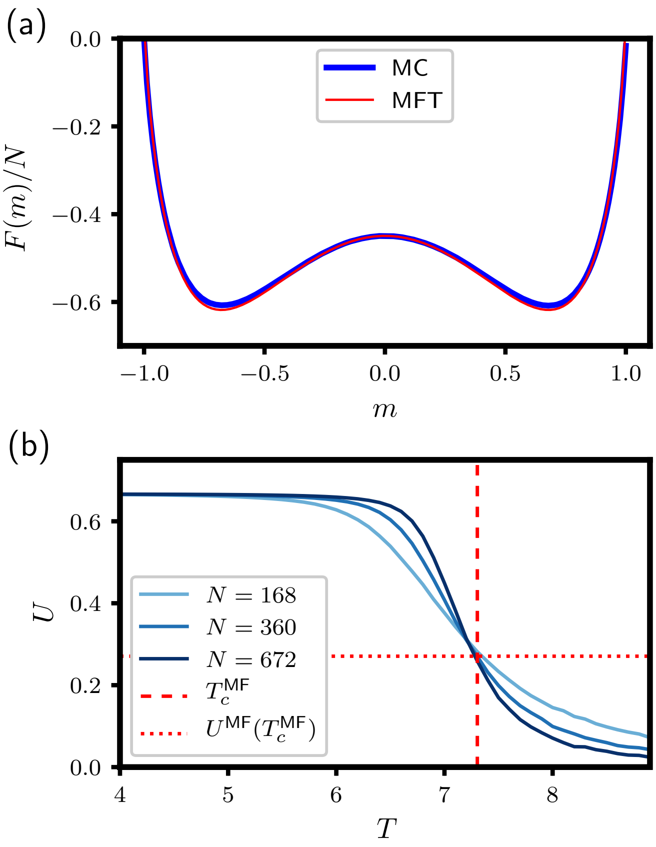

FIG. 2. Comparison between MC and MFT results for the free energy as a function of magnetization and for the critical temperature. (a) Free-energy profile for a periodic triangular lattice with $N = 168$ at $T = 6$, $p = 0$. The MC curve was computed with umbrella sampling for the model of Eq. (2) (see [15] for details), while the MFT curve was obtained from Eq. (22). (b) MFT estimates for the triangular lattice critical temperature $T_c^{\rm MF} = 2\bar{V} \approx 7.31$ and the corresponding value of the Binder cumulant $U^{\rm MF}(T_c^{\rm MF})$ [12] closely predict the intersection point of MC Binder cumulants U for different system sizes. Specifically, MC indicates that $T_c^{\rm MC} \approx 7.2$, so the MFT result is accurate within ≈2%. MC results for the Binder cumulants were computed by sampling 10^6 configurations at each temperature. These configurations were generated using the effective energy function of Eq. (12) rather than Eq. (2) in order to avoid statistical errors associated with insufficient sampling of mechanical fluctuations.

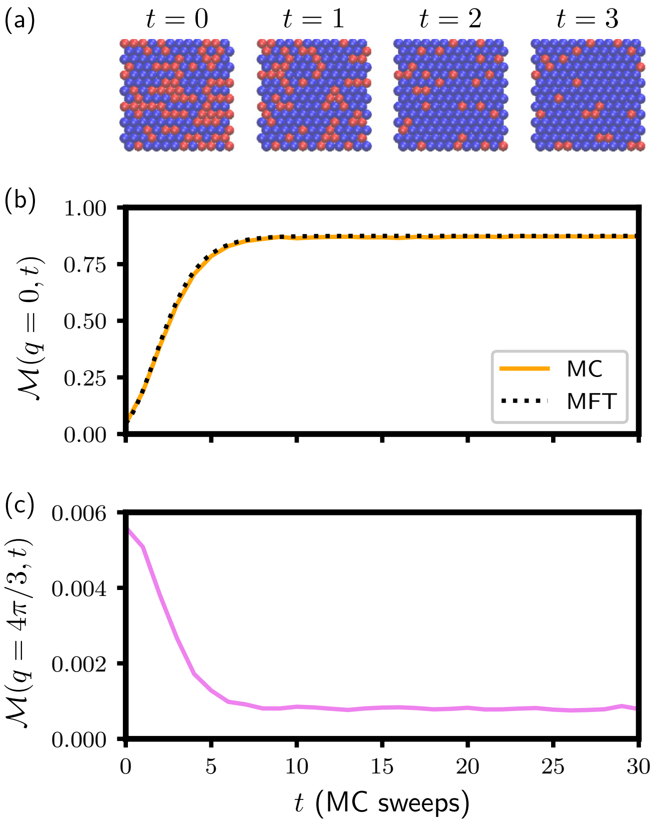

FIG. 3. Magnetization dynamics after a quench from temperature $T_0 = 8$ to $T = 4$ on the triangular lattice. (a) Representative configurations from a single quench trajectory with $N = 168$. The time t following the quench is measured in MC sweeps. (b) Time evolution of the $q = |\mathbf{q}| = 0$ (longest-wavelength) Fourier component of the spin structure factor $\mathcal{M}(\mathbf{q}, t)$ following the quench. This mode grows rapidly at short times and saturates at the equilibrium value of m^2. Solving the mean-field master equation, Eq. (26), for a system size $N = 168$ and initial condition $P(m, 0) = \exp[-F_{\rm MF}(m; T = T_0)/k_B T_0]$ yields a prediction $\mathcal{M}(0, t) = \sum_{m=-1}^{1} m^2 P(m, t)$ (labeled MFT in the plot) which closely agrees with the MC result. (c) Time evolution of a short-wavelength Fourier component of $\mathcal{M}$ with $q = 4\pi/3$ (corresponding to a corner of the first Brillouin zone of the triangular lattice) computed from MC simulations. This mode decays rapidly, consistent with the apparent lack of short-wavelength structure in the configurations. MC curves in both (b) and (c) were obtained by averaging over 10^3 independent trajectories initialized from equilibrium configurations sampled at $T_0 = 8$ and propagated with Metropolis spin-flip dynamics at $T = 4$. All MC simulations here were performed using $\mathcal{H}_{\rm eff}$, Eq. (12).

of spin domains en route to a state of broken symmetry. By contrast, a model with exclusively infinite-range interactions, such as that described by $\mathcal{H}^{\rm LR}$, lacks finite-wavelength spatial correlations entirely and therefore does not exhibit a slowly growing length scale upon quenching. In dynamical simulations of our elastic Ising model, we observe no distinct domain growth upon quenching from $T = 8 > T_c$ to $T = 4 < T_c$, consistent with the observations of Miyashita *et al.* [12]. Indeed, our measurements of the time-dependent spin structure factor $\mathcal{M}(\mathbf{q}, t) = \langle|\tilde{\sigma}(\mathbf{q}, t)|^2\rangle/N^2$ (where $\langle\cdots\rangle$ denotes an ensemble average) show that only the $\mathbf{q} = 0$ mode becomes unstable upon quenching (Fig. 3). This can be understood in detail as a consequence of the energy gap between the $\mathbf{q} = 0$ mode and the finite-wavelength modes depicted in Fig. 1. The lack of participation of the finite-wavelength modes in the quench dynamics suggests that a mean-field framework—in which the only dynamical quantity is the net magnetization—should provide a sensible description of our model's dynamical features. Indeed, a mean-field master equation, which will be described below, predicts the dynamics of $\mathcal{M}(\mathbf{q} = 0, t)$ very accurately [see Fig. 3(b)].

In addition to changes in temperature, one can probe a system's response to a cyclically varying parameter that crosses and recrosses a phase boundary. In the resulting loop, the distinctness of forward and backward branches

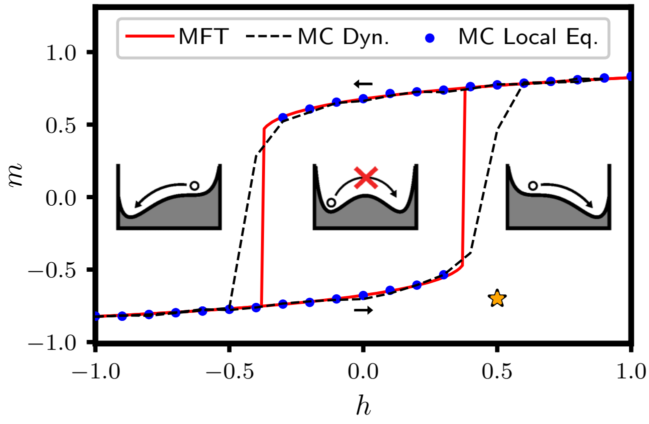

FIG. 4. Hysteresis loop at $T = 6$ from MFT and MC. The MFT curve was obtained by numerical solution of Eq. (21). Solutions to this equation which are also local free-energy minima (of which there are at least one and at most two) comprise the mean-field hysteresis loop. MC Dyn. (dynamic) results were obtained by sweeping the field from $h = -1.0$ to $h = 0.9$ and back again (direction indicated by the black arrows) for a simulated system with $N = 2688$ using $\mathcal{H}_{\text{eff}}$ [Eq. (12)]. For each field value, there were ten MC sweeps of equilibration and ten MC sweeps of production. MC Eq. (equilibrium) results were obtained by locating the local minima of the free energy as a function of magnetization [computed with umbrella sampling using $\mathcal{H}$, Eq. (2)] for different values of h and a system size of $N = 168$. Inset schematics illustrate the fact that, in the thermodynamic limit, barrier crossing does not occur; the system can escape from a metastable well only once it has reached the limits of metastability. The yellow star indicates the values of m and h used as a starting point for dynamics in Fig. 5.

reports on the system's "memory" owing to a slow degree of freedom (the net magnetization, in our case). If such an experiment were performed sufficiently slowly, one would normally expect differences between the two branches to vanish. For our model, hysteresis instead appears to persist for arbitrarily slow cycling. Normally, the free-energy barrier for nucleating a stable phase is subextensive in scale since the thermodynamic cost is interfacial in nature. For our model, finite-size scaling of MC simulation results indicates that the barrier separating minima in $F(m)$ instead scales linearly with system size N. This feature is inherent in MFT, which presumes spatial homogeneity and thus a lack of interfaces. Thermal fluctuations are insufficient to overcome such an extensive barrier in the thermodynamic limit, so the system will persist indefinitely in the state in which it was initialized. The mean-field nature of the barrier in $F(m)$ is reflected in Fig. 4, which shows excellent agreement between hysteresis loops computed from MC and the corresponding prediction of MFT.

At the ends of the hysteresis loop, $F(m)$ is no longer bistable, and a system initialized at the location of the formerly metastable well m_{i} can relax to the single stable well at m_{f} without crossing a barrier. Within MFT, this dynamics can be regarded as a random walk of the magnetization with step length $\Delta m = 2/N$ taken in discrete time steps Δt on the mean-field energy surface. The probability distribution $P(m,t)$ for the magnetization at time t is governed by a master equation [40]:

$$\begin{aligned} P(m,t) = {} & P(m-\Delta m, t-\Delta t)\Pi_+(m-\Delta m) \\ & + P(m+\Delta m, t-\Delta t)\Pi_-(m+\Delta m) \\ & + P(m, t-\Delta t)\{1-[\Pi_+(m)+\Pi_-(m)]\}, \end{aligned} \tag{26}$$

with transition rates

$$\Pi_\pm(m) = \frac{1 \mp m}{2} \min\left[1, e^{-\beta[E_{\text{MF}}(m\pm\Delta m)-E_{\text{MF}}(m)]}\right] \tag{27}$$

for incrementally increasing (decreasing) m. The factor $(1 \mp m)/2$ accounts for the number of available down and up spins, respectively, at magnetization m, which imposes an entropic bias at the mean-field level. These rates satisfy detailed balance with respect to the probability distribution $e^{-\beta F_{\text{MF}}(m)}$. The relaxation process of interest is defined by boundary conditions:

$$P(m,0) = \begin{cases} 1, & m = m_{\text{i}}, \\ 0, & \text{otherwise}, \end{cases} \tag{28}$$

$$P(m_{\text{f}}, t) = 0, \tag{29}$$

ensuring that the system always begins at $m = m_{\text{i}}$ and the magnetization can never exceed $m = m_{\text{f}}$. A different set of boundary conditions was used to compute $\mathcal{M}(0,t)$ for Fig. 3 (details are given in the caption).

Defining the column vector

$$\mathbf{P}(t) = (P(-1,t), P(-1+\Delta m, t), \ldots, P(1,t))^T, \tag{30}$$

where the superscript T denotes the transpose, we can rewrite Eq. (26) as

$$\mathbf{P}(t+\Delta t) = \mathbf{\Omega} \cdot \mathbf{P}(t), \tag{31}$$

where the elements of the transition matrix $\mathbf{\Omega}$ are given by

$$\begin{aligned} \Omega_{m,m'} = {} & \delta_{m,m'}[1-\Pi_+(m)-\Pi_-(m)] \\ & + \delta_{m,m'+\Delta m}\Pi_-(m) + \delta_{m,m'-\Delta m}\Pi_+(m). \end{aligned} \tag{32}$$

Letting $t = n\Delta t$, we can write the formal solution to Eq. (31) as

$$\mathbf{P}(t) = \mathbf{\Omega}^n \cdot \mathbf{P}(0). \tag{33}$$

Numerical propagation of Eq. (33) is straightforward, and with access to $P(m,t)$ we can compute the average magnetization as a function of time,

$$\langle m(t) \rangle = \sum_{m=-1}^{m_{\text{f}}} m P(m,t), \tag{34}$$

as well as the first-passage time distribution $\mathcal{P}(t)$,

$$\mathcal{P}(t) = -\frac{\partial \mathscr{S}(t)}{\partial t}, \tag{35}$$

where the survival probability $\mathscr{S}(t)$ is

$$\mathscr{S}(t) = \sum_{m=-1}^{m_{\text{f}}} P(m,t). \tag{36}$$

We compare the quantities $\langle m(t) \rangle$ and $\mathcal{P}(t)$ to their counterparts computed from MC simulations in Fig. 5. In Fig. 6 we plot first-passage time distributions of relaxation from the

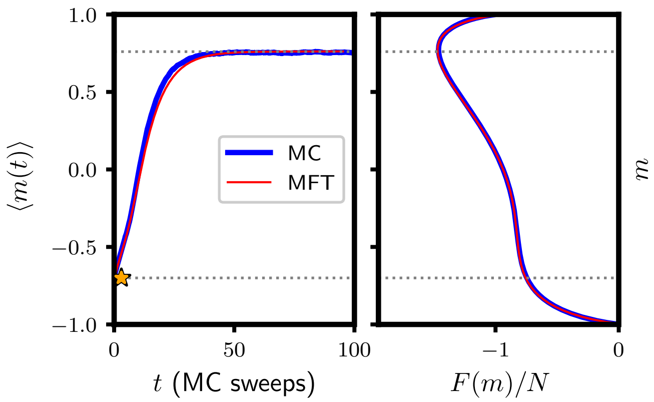

FIG. 5. Average magnetization versus time for phase change dynamics at the end of the hysteresis loop (left) with $T = 6$ and the corresponding free-energy profile (right) with $T = 6$, $h = 0.5$. Gray dashed lines indicate the positions of the formerly metastable well and the single stable well. The yellow star indicates the initial state, marked with the same symbol in Fig. 4. The MFT result for $\langle m(t)\rangle$ was calculated via Eq. (34) for a system size $N = 168$, and the mean-field free energy is given by Eq. (22). The MC result for $\langle m(t)\rangle$ was computed by averaging over 10^4 independent trajectories of a system with $N = 168$. These trajectories were propagated by Metropolis MC according to the effective energy $\mathcal{H}_{\mathrm{eff}}$ [Eq. (12)]. Their initial configurations were sampled from an equilibrium trajectory whose magnetization $m = -0.7$ was fixed by performing Kawasaki dynamics [41]. The MC result for the free energy was computed via umbrella sampling of a system with $N = 168$ using $\mathcal{H}$ [Eq. (2)].

formerly metastable well to the stable well. As is evident in these figures, the dynamics of both the average magnetization and its fluctuations are captured very well by MFT.

V. BOUNDARY EFFECTS IN FINITE CRYSTALS

In our analysis thus far we have assumed periodic boundary conditions. Any real crystal is, of course, terminated with surfaces, edges, and corners. The special physical and chemical properties of nanoscale materials [43], in which a sizable fraction of atoms lies at the periphery, highlight the diverse influences of such boundary features. As one relevant example, experiments on [44,45] and simulations of [46–49] spin-crossover compounds indicate that boundaries can provide preferred sites for nucleation of low-spin or high-spin phases. While some of these studies were performed in crystalline excerpts nearly macroscopic in size [45], the setting of many recent studies has been nanocrystals [50–53], where the impact of the boundary on material properties ought to be particularly acute. We therefore studied the impact of open boundary conditions on our model, with an emphasis on "nanoscale" systems that span just tens of lattice spacings.

While the analysis of fluctuations in δa is insensitive to the choice of boundary conditions, broken translational invariance means that a Fourier transform will not diagonalize $\Delta\mathcal{H}$. As a result, the required integrals in Eq. (11) are more complicated but still numerically tractable. For a given nanocrystal size and shape, they can be performed numerically exactly to yield an effective Hamiltonian:

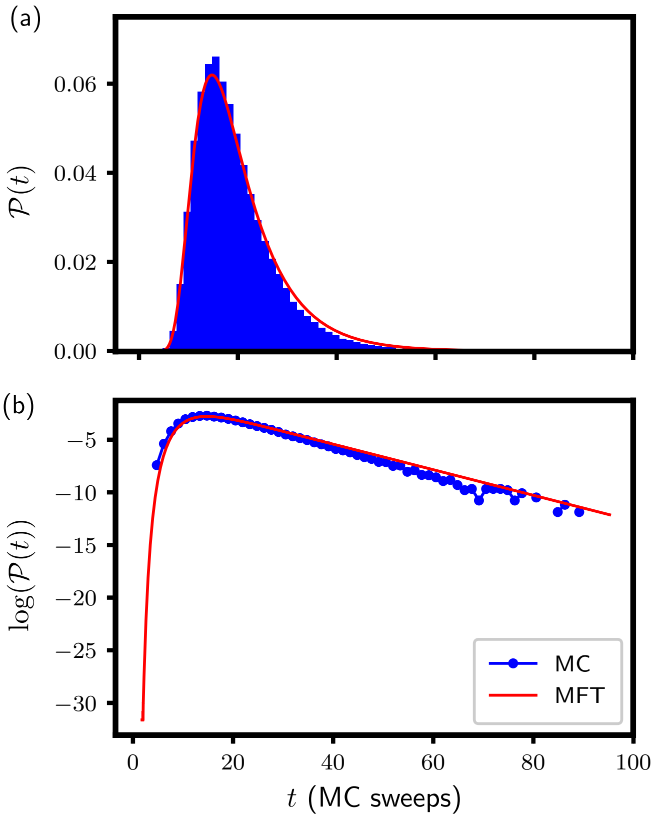

FIG. 6. Probability distribution of the first-passage time for phase change at the end of the hysteresis loop with $T = 6$, plotted on (a) linear and (b) logarithmic scales. For each MC trajectory, the first-passage time was defined as the number of MC steps taken en route from the formerly metastable initial state ($m = -0.7$) to the bottom of the stable well ($m = 0.76$). Results are shown for a system of size $N = 168$. MFT predictions were computed via Eq. (35) for the same system size. The long-time exponential tail is characteristic of diffusion on a bounded interval; its corresponding decay rate is set by the least negative eigenvalue of $\boldsymbol{\Omega}$ [42]. The entire eigenvalue spectrum of $\boldsymbol{\Omega}$ is sensitive to changes in N, highlighting the size dependence of first-passage time statistics that appears to be well captured by MFT.

$$\mathcal{H}_{\mathrm{eff}} = \frac{1}{2}\sum_{\mathbf{R},\mathbf{R}'} \sigma_{\mathbf{R}} V_{\mathbf{R},\mathbf{R}'} \sigma_{\mathbf{R}'} - h \sum_{\mathbf{R}} \sigma_{\mathbf{R}}, \tag{37}$$

where due to broken translational symmetry, the effective potential depends on both $\mathbf{R}$ and $\mathbf{R}'$, not just their difference. Plots of this potential for a hexagonally shaped nanocrystal with triangular lattice structure are shown in Fig. 7. Interactions between sites towards the interior of the crystal closely resemble bulk interactions, although interactions between sites towards the perimeter of the crystal differ significantly from bulk interactions (see [14]). These surface interactions lead to lower energies for compositional defects located on the perimeter as opposed to the interior of the crystal [15], consistent with studies reporting nucleation near the surface of spin-crossover crystals [46,48,49]. Importantly, the interior interactions largely retain the long-range component, meaning that MFT might still prove reasonably accurate. Unlike in the

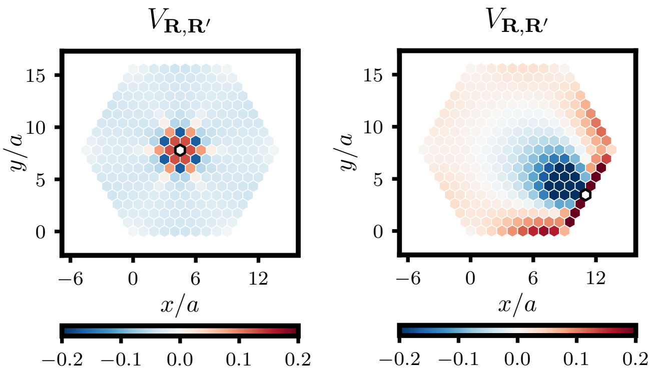

(a) Tagged atom at center. (b) Tagged atom on edge.

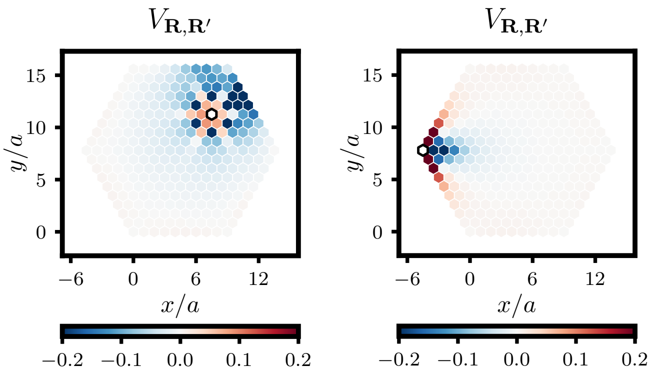

(c) Tagged atom between center and edge. (d) Tagged atom at corner.

FIG. 7. Pair interaction function $V_{\mathbf{R},\mathbf{R}'}$ for different locations $\mathbf{R}$ of a tagged atom (outlined in black). The value of $V_{\mathbf{R},\mathbf{R}'}$ for interaction with another atom at $\mathbf{R}'$ is indicated by color according to the scale shown.

bulk, sites in the nanocrystal do not all experience the same average environment. An accurate MFT must take this spatial variation into account. A set of self-consistent equations for the average magnetization $m_\mathbf{R}$ of each site in the nanocrystal can be written as [15]

$$m_\mathbf{R} = \tanh\left(-\beta \sum_{\mathbf{R}'\neq\mathbf{R}} V_{\mathbf{R},\mathbf{R}'} m_{\mathbf{R}'}\right). \tag{38}$$

An example of solutions to this set of equations, computed using the same techniques as in [14], is shown in Fig. 8. The average net magnetization is then simply computed as

$$m = \frac{1}{N}\sum_{\mathbf{R}} m_\mathbf{R}. \tag{39}$$

We used Eqs. (38) and (39) to compute mean-field predictions for m as a function of temperature for hexagonal nanocrystals of different sizes. Due to this finite size, thermal fluctuations will cause the system to cross the barrier separating degenerate free-energy minima increasingly frequently as T_c is approached from below, so that straightforward averaging of an equilibrium MC trajectory will result in $m \approx 0$. In order make a comparison to MFT predictions, we instead computed MC estimates for $m(T)$ by locating the minima of free-energy profiles computed with umbrella sampling. MC results obtained in this way correspond quite closely with MFT predictions (see Fig. 9), consistent with long-range interactions in the nanocrystal effective potential. Furthermore, we found that the height of the nanocrystal free-energy barrier computed from umbrella sampling MC simulations for $T < T_c$ scales linearly with system size N, just as in the bulk (see Fig. 10). We thus anticipate a similar agreement between MFT and MC for nanocrystal dynamics.

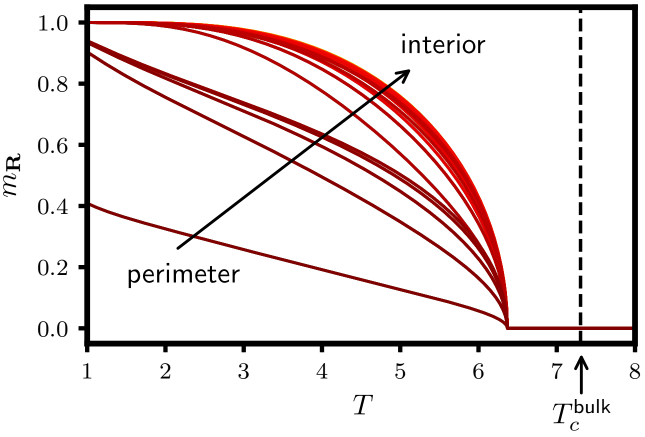

FIG. 8. Numerical solutions to Eq. (38) for the position-dependent mean-field magnetization of a hexagonal nanocrystal of size $N = 271$ with triangular lattice structure. Curves with different shades of red represent the magnetization of different sites in the nanocrystal. Sites near the perimeter of the crystal have smaller magnetization than sites well within the interior; all sites transition from zero to nonzero magnetization at a temperature $T_c \approx 6.2$. The vertical dashed line marks the bulk value for T_c; open boundary conditions thus suppress the nanocrystal T_c compared to its bulk value.

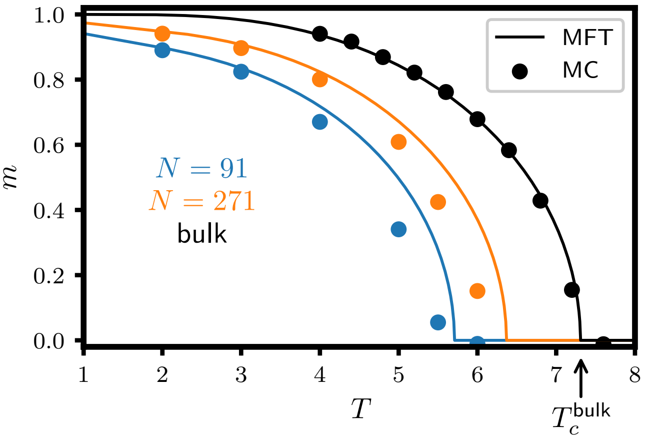

FIG. 9. Nanocrystal magnetization as a function of temperature for different system sizes. Bulk magnetization versus temperature (for a system with $N = 168$ subject to periodic boundary conditions) is included for comparison. Nanocrystal MFT curves were obtained as the numerical solutions of Eqs. (38) and (39). Nanocrystal MC points were obtained as the minima of free-energy profiles computed via umbrella sampling of the effective Hamiltonian, Eq. (37), for each system size. The bulk MFT curve was computed using Eq. (21), and bulk MC points were obtained from bulk free-energy minima computed via umbrella sampling using Eq. (2).

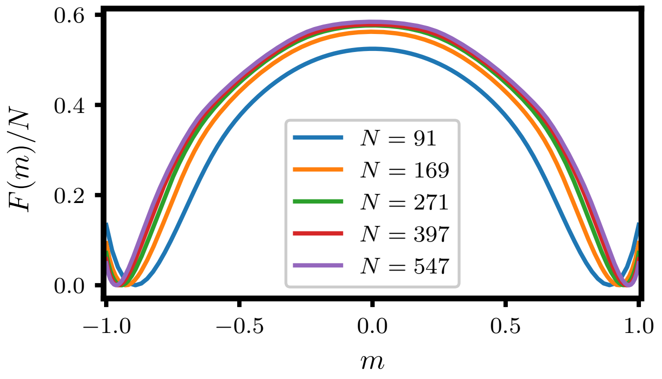

FIG. 10. Nanocrystal free energies per atom for different system sizes at $T = 3$, $h = 0$. Curves were computed via umbrella sampling of the effective Hamiltonian, Eq. (37), for each system size. These profiles strongly suggest a free-energy barrier which grows linearly with N.

VI. ENSEMBLE INEQUIVALENCE

We have thus far sidestepped a subtle, but important, caveat. Specifically, while the factor of $1/N$ in V^{LR} ensures that the energy is extensive, the arbitrarily long interaction range means that the energy is no longer additive [54,55]. In turn, this means that derivatives of the free energy $F(m)$ no longer have a definite sign, and hence, its Legendre transform is no longer a single-valued function [56]. In other words, the ensemble in which m is fixed and the ensemble in which m can fluctuate are no longer equivalent [57]. Thus, the modulated structures observed in an ensemble with fixed magnetization—as in our previous work [14]—are not equilibrium states in the present ensemble, where the net magnetization can fluctuate.

VII. CONCLUSION

Our findings have significant implications for functional elastic materials. We have shown that long-range interactions are a generic consequence of elastic fluctuations in lattice-mismatched solids. They should thus be operative, for instance, in spin-crossover compounds. One of the intriguing features of these compounds is the enhanced metastability of their high-spin-rich and low-spin-rich phases near room temperature [6,50,58,59], which makes them promising for use as molecular switches in next-generation data storage devices. Our results provide an underlying reason for this behavior: the extensive free-energy barrier separating the two phases means that spin-crossover materials are robust to fluctuations typically responsible for the decay of metastable states. This barrier scaling also explains why transitions between high- and low-spin phases under an applied field are macroscopically sharp. We thus anticipate that our MFT will provide a simple, quantitative framework in which to explain and predict further properties of these materials.

ACKNOWLEDGMENTS

We thank J. H. H. Perk for helpful comments on an earlier version of this paper. This work was supported by National Science Foundation (NSF) Grant No. CHE-1416161. This research also used resources of the National Energy Research Scientific Computing Center (NERSC), a US Department of Energy Office of Science User Facility operated under Contract No. DE-AC02-05CH11231. P.L.G. and L.B.F. acknowledge stays at the Erwin Schrödinger International Institute for Mathematics and Physics (ESI).

---

[1] O. K. Rice, J. Chem. Phys. **22**, 1535 (1954).
[2] C. Domb, J. Chem. Phys. **25**, 783 (1956).
[3] G. A. Baker and J. W. Essam, Phys. Rev. Lett. **24**, 447 (1970).
[4] J. Oitmaa and M. N. Barber, J. Phys. C **8**, 3653 (1975).
[5] J.-F. Létard, L. Capes, G. Chastanet, N. Moliner, S. Létard, J.-A. Real, and O. Kahn, Chem. Phys. Lett. **313**, 115 (1999).
[6] A. Hauser, J. Jeftić, H. Romstedt, R. Hinek, and H. Spiering, Coord. Chem. Rev. **190–192**, 471 (1999).
[7] J. A. Real, A. B. Gaspar, and M. C. Muñoz, Dalton Trans. **12**, 2062 (2005).
[8] P. Gutlich, V. Ksenofontov, and A. Gaspar, Coord. Chem. Rev. **249**, 1811 (2005).
[9] Y. Konishi, H. Tokoro, M. Nishino, and S. Miyashita, Phys. Rev. Lett. **100**, 067206 (2008).
[10] B. Dünweg and D. P. Landau, Phys. Rev. B **48**, 14182 (1993).
[11] E. M. Vandeworp and K. E. Newman, Phys. Rev. B **55**, 14222 (1997).
[12] S. Miyashita, Y. Konishi, M. Nishino, H. Tokoro, and P. A. Rikvold, Phys. Rev. B **77**, 014105 (2008).
[13] S. Miyashita, P. A. Rikvold, T. Mori, Y. Konishi, M. Nishino, and H. Tokoro, Phys. Rev. B **80**, 064414 (2009).
[14] L. B. Frechette, C. Dellago, and P. L. Geissler, Phys. Rev. Lett. **123**, 135701 (2019).
[15] See Supplemental Material at http://link.aps.org/supplemental/10.1103/PhysRevB.102.024102, which includes Refs. [50–52,60–62], for details of additional calculations and Monte Carlo simulations.
[16] Note that we have dropped δ in front of $\tilde{\sigma}_{\mathbf{q}}$. That is because $\delta\tilde{\sigma}_{\mathbf{q}} = \tilde{\sigma}_{\mathbf{q}} - \delta_{\mathbf{q},0}\tilde{\sigma}_0$, but $\tilde{V}_0 = 0$, so $\tilde{\sigma}_0$ simply does not contribute to the sum.
[17] D. Dantchev and J. Rudnick, Eur. Phys. J. B **21**, 251 (2001).
[18] E. M. Stein and R. Shakarchi, *Complex Analysis* (Princeton University Press, Princeton, NJ, 2003).
[19] The function $V^{\mathrm{SR}}_{\mathbf{R}}$ is generally anisotropic; for the triangular lattice, its slowest decay is $1/|\mathbf{R}|^4$ along (certain linear combinations of) triangular lattice basis vectors [14].
[20] N. Willenbacher and H. Spiering, J. Phys. C **21**, 1423 (1988).
[21] H. Spiering and N. Willenbacher, J. Phys.: Condens. Matter **1**, 10089 (1989).
[22] C. P. Köhler, R. Jakobi, E. Meissner, L. Wiehl, H. Spiering, and P. Gütlich, J. Phys. Chem. Solids **51**, 239 (1990).
[23] K. Boukheddaden, I. Shteto, B. Hôo, and F. Varret, Phys. Rev. B **62**, 14796 (2000).

[24] K. Boukheddaden, I. Shteto, B. Hôo, and F. Varret, Phys. Rev. B **62**, 14806 (2000).

[25] H. Fourati, E. Milin, A. Slimani, G. Chastanet, Y. Abid, S. Triki, and K. Boukheddaden, Phys. Chem. Chem. Phys. **20**, 10142 (2018).

[26] B. J. Schulz, B. Dünweg, K. Binder, and M. Müller, Phys. Rev. Lett. **95**, 096101 (2005).

[27] M. Kac, G. E. Uhlenbeck, and P. C. Hemmer, J. Math. Phys. **4**, 216 (1963).

[28] S. A. Cannas, A. C. N. de Magalhães, and F. A. Tamarit, Phys. Rev. B **61**, 11521 (2000).

[29] B. B. Vollmayr-Lee and E. Luijten, Phys. Rev. E **63**, 031108 (2001).

[30] T. Mori, Phys. Rev. E **82**, 060103(R) (2010).

[31] H. W. Capel, L. W. J. den Ouden, and J. H. H. Perk, Phys. A (Amsterdam, Neth.) **95**, 371 (1979).

[32] T. Nakada, P. A. Rikvold, T. Mori, M. Nishino, and S. Miyashita, Phys. Rev. B **84**, 054433 (2011).

[33] M. Nishino and S. Miyashita, Phys. Rev. B **88**, 014108 (2013).

[34] M. Nishino, C. Enachescu, and S. Miyashita, Phys. Rev. B **100**, 134414 (2019).

[35] D. Chandler, *Introduction to Modern Statistical Mechanics* (Oxford University Press, New York, 1987).

[36] G. M. Torrie and J. P. Valleau, J. Comput. Phys. **23**, 187 (1977).

[37] S. Kumar, J. M. Rosenberg, D. Bouzida, R. H. Swendsen, and P. A. Kollman, J. Comput. Chem. **13**, 1011 (1992).

[38] K. Binder, Phys. Rev. Lett. **47**, 693 (1981).

[39] J. W. Cahn, J. Chem. Phys. **42**, 93 (1965).

[40] Mean-field dynamics can also be accessed by directly simulating the MC dynamics of a mean-field Hamiltonian; see [15] for details.

[41] K. Kawasaki, Phys. Rev. **145**, 224 (1966).

[42] S. Redner, *A Guide to First-Passage Processes* (Cambridge University Press, Cambridge, 2001).

[43] M. V. Kovalenko, L. Manna, A. Cabot, Z. Hens, D. V. Talapin, C. R. Kagan, V. I. Klimov, A. L. Rogach, P. Reiss, D. J. Milliron, P. Guyot-Sionnest, G. Konstantatos, W. J. Parak, T. Hyeon, B. A. Korgel, C. B. Murray, and W. Heiss, ACS Nano **9**, 1012 (2015).

[44] S. Pillet, V. Legrand, M. Souhassou, and C. Lecomte, Phys. Rev. B **74**, 140101(R) (2006).

[45] A. Slimani, F. Varret, K. Boukheddaden, C. Chong, H. Mishra, J. Haasnoot, and S. Pillet, Phys. Rev. B **84**, 094442 (2011).

[46] C. Enachescu, L. Stoleriu, A. Stancu, and A. Hauser, Phys. Rev. Lett. **102**, 257204 (2009).

[47] C. Enachescu, M. Nishino, S. Miyashita, L. Stoleriu, and A. Stancu, Phys. Rev. B **86**, 054114 (2012).

[48] C. Enachescu, M. Nishino, S. Miyashita, K. Boukheddaden, F. Varret, and P. A. Rikvold, Phys. Rev. B **91**, 104102 (2015).

[49] M. Nishino, C. Enachescu, S. Miyashita, P. A. Rikvold, K. Boukheddaden, and F. Varret, Sci. Rep. **1**, 162 (2011).

[50] I. Boldog, A. B. Gaspar, V. Martínez, P. Pardo-Ibañez, V. Ksenofontov, A. Bhattacharjee, P. Gütlich, and J. A. Real, Angew. Chem. Int. Ed. **47**, 6433 (2008).

[51] I. Gudyma, V. Ivashko, and A. Bobák, Nanoscale Res. Lett. **12**, 101 (2017).

[52] C. Enachescu and W. Nicolazzi, C. R. Chim. **21**, 1179 (2018).

[53] M. Mikolasek, K. Ridier, D. Bessas, V. Cerantola, G. Félix, G. Chaboussant, M. Piedrahita-Bello, E. Angulo-Cervera, L. Godard, W. Nicolazzi, L. Salmon, G. Molnár, and A. Bousseksou, J. Phys. Chem. Lett. **10**, 1511 (2019).

[54] T. Mori, Phys. Rev. Lett. **111**, 020601 (2013).

[55] A. Campa, T. Dauxois, and S. Ruffo, Phys. Rep. **480**, 57 (2009).

[56] R. K. P. Zia, E. F. Redish, and S. R. McKay, Am. J. Phys. **77**, 614 (2009).

[57] In a related context, Vandeworp and Newman [11] previously noted inequivalence between canonical and grand-canonical ensembles for a Keating model of a semiconductor mixture.

[58] S. Hayami, Z.-z. Gu, H. Yoshiki, A. Fujishima, and O. Sato, J. Am. Chem. Soc. **123**, 11644 (2001).

[59] M. Paez-Espejo, M. Sy, and K. Boukheddaden, J. Am. Chem. Soc. **140**, 11954 (2018).

[60] M. Matsumoto and T. Nishimura, ACM Trans. Model. Comput. Simul. **8**, 3 (1998).

[61] F. R. M. Galassi, J. Davies, J. Theiler, B. Gough, G. Jungman, P. Alken, and M. Booth, *GNU Scientific Library Reference Manual*, 3rd ed. (Network Theory, Bristol, UK, 2009).

[62] D. Frenkel and B. Smit, *Understanding Molecular Simulation: From Algorithms to Applications*, 2nd ed. (Academic, San Diego, 2001), Chap. 7.